Supernova Plasma Effects

P. Marko
SXM Innovation Center
Correspondence: pmarko@siriusxm.com

Simulations based on extragalactic supernova (SN) observations predict during active epochs several SN explosions (SNe) can occur within the Milky Way galaxy every century. A review of observational data collected on the Circumgalactic Medium (CGM) provides support for the existence of a class of SN originating as runaway OB stars or halo stars exploding in a rarified environment outside of the Interstellar Medium (ISM). Unlike most SN which explode within the ISM where the ambient gas generally absorbs blast waves within a million years, the blast waves from this class of SN propagate in a rarified medium and can remain in a high velocity free expansion phase for more extended periods. These high velocity blast waves are analyzed with a focus on their potential to influence celestial observations. The SN blast wave physical properties, such as the relative permittivity and permeability, are investigated and found to exhibit values outside the traditional bounds with ranges capable of altering the propagation of light. These plasma properties, when incorporated into dynamic SN blast wave models, are shown to induce reflections and redshifts to propagating light fields which can appear to observers as common cosmological phenomena such as elliptical galaxies, gravitational lenses and the Hubble constant.

Keywords: Supernova, Plasma, Gravitational Lens, Hubble Constant

1. Introduction

Ongoing technical advances in sensors, telescopes and light processing algorithms are enabling observations deeper into the universe with higher image clarity and better spectrum resolution of objects in the light field. These advances continue to expose additional details prompting the development of new or refined models and theories to better align with the data. In general, objects appearing in the light field are accepted as being present at or near the observed position in space and any change to the light spectrum rest frequency is credited to Doppler shifts. While plasmas have been observed to impact the propagation of electromagnetic (EM) waves in the atmosphere with global navigation systems operating at L-band, well known equations for the index of refraction predict plasmas are transparent at and above light frequencies (*1*). More recent measurements of ionic plasmas using soft x-rays uncovered an unexpected increase in the index of refraction which prompted the development of a new method for calculating the index in ionic plasmas (2). Moreover, high velocity plasmas are known to exhibit diamagnetism ($\mu_r < 1$) in static magnetic fields, and this property also applies to the magnetic field of an incident EM wave (*3*). However, a more detailed analysis of EM wave forces on high velocity plasma shows under some conditions the plasma becomes paramagnetic. Additionally, a novel dynamic propagation environment for altering the rest frequency has been identified where changes in the index of refraction between stationary endpoints can induce redshifts. These developments warranted a closer look at how space plasmas can influence celestial observations. SNe are a major source of galactic plasma and low rate occurrences in a rarified halo or CGM have been modeled to demonstrate their potential to impact galactic and extragalactic observations. The modeled blast waves being optically thin are very difficult to detect and direct evidence under non-shock conditions has not been reported in the observational data. However, measurements of the Milky Way halo and the halos and CGMs of external galaxies are reviewed and found to provide indirect evidence to support their existence. The blast waves modeled with paramagnetic plasma properties are shown to mirror the characteristics of common celestial phenomena including dim elliptical galaxies, gravitational lenses and the Hubble Constant.

2. Supernova Blast Wave Model and Expansion Medium

Most of what is known and theorized about the SNe comes from photometric observations. The progenitors of SNes vary widely and can strongly influence the Circumstellar Medium (CSM) which impacts the early phase of the blast wave. Type II SN progenitors may be massive hot stars expelling large amounts of mass in fast stellar winds. At the time the SN explodes it may be surrounded by a low density bubble encompassed in a thin dense shell formed by the wind interacting with the ISM. If the progenitor is a Red Supergiant (RSG) with a slower steady state wind when the star explodes, the profile of the density ρ will be $\rho \propto r^{-2}$. The progenitor may explode without evolving to a RSG or the RSG may contract prior to exploding creating more complex CSM and ISM interactions and structures (*4-6*).

Observations of Type Ia SNe affirm the explosions typically rise to maximum light in approximately 20 days, followed by a first rapid declining of about 3 orders of magnitude in approximately 30 days and then an exponential decay of one order of magnitude per month. Analysis of early phase spectra of Type Ia SN indicate the expanding ejecta is comprised of neutral and ionized intermediate-mass elements (O, Mg, Si, S, Ca) with some contribution from iron-peak elements (Fe, Ca) (*7*).

To a good approximation, the exploding material on the SN can be modeled as a fully ionized plasma (*8*). Theoretical hydrodynamic explosion models for Type Ia SN have been developed based on observed light curves and spectra. While the models predict early phase ejecta velocities range from less than 100 km s^{-1} to over 25,000 km s^{-1}, multiple models predict a high density of ejecta material tightly grouped near 10,000 km s^{-1} (*9*).

Extensive research has been conducted on the evolution of the SNBW and in general for a SNe within the ISM the expanding ejecta can be segmented into multiple phases as it interacts with the surrounding media (*4,10*). This interaction begins in the Pre-Sedov-Taylor Phase which is characterized initially by free expansion where the SN ejecta moves radially outward at velocities in the range of 10^4 km s^{-1}. The ejecta leaves the star as a pressure pulse and transitions to a shock wave when it encounters gas in the CSM and ISM. The shock wave is characterized by a discontinuity in pressure which propagates through the gas and for simplicity can be modeled with a Friedlander waveform (*11*) described by

$$P(t) = P_s e^{\frac{-t}{t_a}}(1 - \frac{t}{t_a}) \qquad (1)$$

where $P(t)$ is the pressure versus time at a point in space, P_s is the overpressure and t_a is the time it takes for the overpressure to return to ambient pressure, as shown in Fig. 1 as a function of distance.

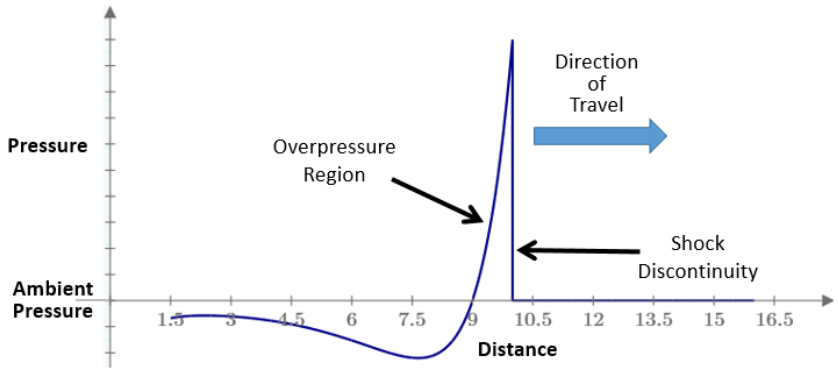

Fig. 1. SNBW pressure versus distance plot

Referring to Fig. 1, the shock discontinuity forms in ambient gas when the higher pressure portion of the pressure pulse catches up with the slower moving leading edge causing the leading edge to steepen. The behavior of the plasma across the discontinuity is defined by a set of jump conditions which constrain the fluid parameters and EM parameters to conserve mass, momentum and energy (*12*). The width of the blast wave in Fig. 1 is defined as the radial length the overpressure region remains above ambient pressure. As the blast wave expands with time, the width also expands due to variations in particle velocity and other factors discussed later.

Continuing in the Pre-Sedov-Taylor Phase, as the ejecta propagates into the ISM it shocks the gas and begins to sweep up interstellar material. The shock wave radius R expands with time t as $R \propto t$ during this phase and some ejecta kinetic energy is converted to heat. When the swept up mass is comparable to the initial mass of the ejecta approximately 70% of the initial energy has been converted to thermal energy and the shock wave enters the Sedov-Taylor Phase.

The Sedov-Taylor Phase is an energy conserving phase and the shock wave radius expands adiabatically with $\propto t^{\frac{2}{5}}$. Additional mass is swept up during this phase and the radial momentum increases. As the shock wave continues to expand, the temperature of the shock wave drops due to radiative cooling and a transition to the P. D. Snow Plow Phase begins. Radiative losses increase and as the shock front slows, higher velocity post-shock gas compresses behind the shock front to form a dense shell to begin the P. D. Snow Plow Phase. During the P. D. Snow Plow Phase, as the expanding dense shell continues to cool and sweep up interstellar material the shock velocity drops and the overall radial momentum drops. Finally, the Momentum-Conserving Snow Plow Phase begins once the shock front cools and the momentum of the shell is conserved. This phase eventually ends when the velocity of expansion drops to the sound speed of the ISM and the shock wave transitions to an acoustic wave. At this point the SN Remnant (SNR) has blended with the ISM and is no longer detectable. The time the SNBW remains in any of the phases is directly related to the characteristics of the surrounding ISM and in a non-homogeneous medium it is possible for some portions of the blast wave to simultaneously exist in different phases and at different distances from the blast center.

SNes provide an important feedback function to balance star formation in multiple models of disk galaxies (*13-15*). SNe winds and outflows heat and redistribute material from the center of the galaxy to the outer regions and beyond and in galaxy models the process helps to reduce star formation to levels aligned with cosmic observations. The galactic winds driven by SNe also play a role in driving material into the Intergalactic Medium (*16*). SNe-driven outflows can occur when multiple SNes are correlated in space and time such that the SNRs overlap and create superbubbles in the ISM (*17,18*). These superbubbles can grow large enough to break out of the ISM disk and enable outflows of SNR material to escape into the CGM at velocities of up to several hundred km s^{-1} (*19*). Another mechanism by which SNe-driven outflows can drive material into the IGM occurs if the SN explodes in a region of the galaxy where the ISM is very thin. In spiral galaxies, the ISM disk can extend above the galactic plane by 500 pc or more (*20*) before the density significantly drops. In observations of H II bubbles in galaxy M33, larger and more spherical bubbles have been detected with increasing galactocentric distance (*21*) indicative of the ISM thinning toward the outer edge of the ISM disk. Measurements of the ISM in elliptical galaxies show variations ranging from some galaxies having disturbed non-uniform ISMs (*22*) to others having ISMs which become increasingly thinner with galactocentric radius (*23*) to others with rare or missing ISMs (*24,25*). Extragalactic statistics of SNe indicate elliptical galaxies have fewer SNe than spirals but the elliptical SNe rate per luminosity may be highest in halo stars which are generally in the outer thinner regions of the ISM (*26*).

The Kepler SNe is an example of a high above plane SN estimated to be at a distance ranging from 2.5 kpc to 12 kpc and a height above the galactic plane ranging from 380 pc to 1.4 kpc with more recent measurements favoring the lower end of the height range (*27-29*). However, Kepler SN is not typical of an SNe in a rarified medium outside the ISM as Chandra observations show the Kepler ejecta spectra heavy with metallic ions indicating Kepler likely exploded in a dense CSM. The observations conflict with Kepler originating as a halo star or a runaway OB star or binary system as these are inconsistent with CSM abundancies (*30*), but the heavy CSM interaction and close proximity to the ISM are in alignment with the observed ejecta velocities.

In spiral galaxies, hydrodynamic simulations support the height of the SNe relative to the ISM is a major factor impacting the SNe-driven outflow (*16*). When a SN explodes in the halo or in the CGM outside the ISM, referred to as a Circumgalactic SN (CG-SN) hereafter, as the shock wave leaves the CSM into the rarified CGM, the ejecta moving away from the galaxy encounters a CGM which is thinning with distance resulting in a shock wave which never sweeps up enough material to enter the Sedov-Taylor Phase. The ejecta moving toward the galaxy encounters the ISM and follows the SNBW evolution for SNes within the ISM. For the ejecta moving away from the galaxy, it is theorized the CG-SN blast wave energy converted to heat during the early phase rapidly cools as the blast wave expands at a velocity in the range of 10,000 km s^{-1}. The blast wave expanding into the rarified CGM is very difficult to detect as an ambient density of $>10^{-3}$ cm^{-3} is required to generate an observable radio emission (*31*).

CG-SNs are expected to comprise a very small percentage of the total SN occurrences. Based on extragalactic observations, models have been developed which estimate a total galactic SN rate of ~4.6 per century (*32*). With the Circumgalactic Blast Wave (CG-BW) expanding at an average velocity of 0.025C, and with the Milky Way Galaxy at approximately 100k light years in diameter, for a CG-SN explosion occurring near the galactic center it would take approximately 50k/0.025 = 2 million years for the CG-BW to expand to the edge of the galaxy. If the SN rate of 4.6 per century is assumed constant during active SN epochs, approximately 92,000 SN explosions would have occurred during this period. Estimating substantially less than 1 in 1000 are either runaway OB stars or halo stars exploding as CG-SNs, less than 100 CG-BWs would be in a high velocity free expansion state traveling radially outward within a reference sphere encompassing the galaxy. As the SN rate changes over the evolution of the galaxy, in epochs of low SN activity the CGM may be void of CG-BWs in a free expansion state.

Observational evidence from Lyman Break Galaxies supports the CGM may be very thin near the galaxy as over millions of years SN-driven winds drive away intergalactic gas (*33,34*). It has been estimated these outflows evacuating CGM material continue out to a galactopause at a range of 100-200 kpc where the outflows stall. The virial radius where this dynamic equilibrium happens in the Milky Way is estimated at 153 kpc (*35*) which is well beyond the CG-BW expansion ranges considered here. These estimates are supported by the COS-Halos Survey, where at these distances high metallicity ionized gas has been observed in the CGM of multiple low-redshift galaxies (*36*). The galactic superwinds driving these outflows are difficult to observe and have implied wind fluid velocities of up to 3k km s^{-1} (*37-39*). For the Milky Way, observations support the halo in the inner galaxy is comprised of irregular small and large scale structures of gas with large variations in temperature, density, composition and velocity (*40,41*). Additional spectrographic studies of the Milky Way halo show many of the clouds consist of highly ionized high velocity gas, referred to as high velocity clouds (HVCs) (*42*). As most HVC detection is based on line-of-sight absorption imprints on the relatively smooth continua of QSOs or low-redshift Type I Seyfert Galaxy nuclei, additional information is required to determine the distance to the HVCs, although it is generally accepted that much of the HVCs occur at large scale heights above the galactic plane. Observational constraints of many ionized HVCs lead to the conclusion that collisional

ionization is most probably the dominant ionization process (*43*). Major theories for the origins of HVCs include 1) gas from the galactic disk being injected into the halo such as superbubble break outs and being further energized by stellar winds from young stars or SNes, 2) inflow of material from satellite galaxies such as the Magellanic Stream where some on the gas is tidally stripped and falls toward the galaxy disk and 3) dark matter-dominated gas clouds which flow along galactic filaments which fall toward the galaxy disk (*44*). HVCs can be interpreted as evidence for the presence of CG-BWs in the halo as the high velocity ejecta can both collisionally ionize the clouds and drive the cloud kinetic energy (*45*). These cloud interactions will create regions of low density or holes in the hemispherical surface of the free expanding CG-BW. In the Milky Way, halo observations show at galactocentric radii $R < 3$ kpc and a height above plane $z > 500$ pc there is virtually no gas detected which is consistent with the model that SN superwinds have driven out the gas over the range of 1-4 kpc (46). For galactocentric radii R between 4 kpc and 8 kpc the halo between clouds becomes more quiescent with a density which drops exponentially with distance from the galactic plane.

Due to the low estimated rate of CG-SNs, the relatively short time window for detection before the ejecta becomes optically thin and the limitations in observations of the ISM and gaseous halo, direct evidence of a CG-BW is generally rare and subject to misinterpretation. A CG-SN with initial mass of 1 $M_{\odot}$ in free expansion may reach a radius of 200 LY within 10k years and with a shell thickness expansion rate 10% of the radial velocity, the ion particle density will already be below 10^{-4} cm^{-3} with a column density $<10^{15}$ cm^{-2}. The presence of multiple ion species in combination with a large velocity dispersion further reduces detectability by absorption spectroscopy. An absorption spectral imprint measured along a path normal to the wave surface with a uniform ion velocity dispersion of 1k km s^{-1} would be suppressed 20dB relative to an imprint of the same column density with a velocity dispersion equal to 10 km s^{-1}. An absorption measurement along a path tangent to the wave surface would not capture the true expansion and dispersion velocities and could be misinterpreted as an HVC cloud. Finding evidence of CG-SNs in gaseous halos is problematic as halos can be very extended with low surface brightness making them difficult to find. For example, a radio continuum survey of 181 nearby inclined galaxies showed only 7 with measurable emissions at high-z above the galactic plane (*47*). For gaseous halo observations, since it is difficult to separate emissions coming from the galaxy disk and halo, observations on inclined galaxies are preferred at a cost of limiting kinematic information on the halo gas. In face-on extragalactic observations of the ISM, Hα surveys can provide evidence of recent SNe activity in close proximity to the galactic plane, but information on the height above the plane is not available. For example, in a survey of M33, multiple H II spherical bubbles have been detected but without enough information to conclude any one of the imprints were from an above plane CG-SN (*21*). Above the galactic plane, large shells and super shells have been observed which are hemispherical and exhibit mass and kinetic energies far greater than a single SN (*48,49*). Some of these shell structures can be created by CG-SNs efficiently transferring energy to nearby dense gaseous clouds.

Within the Milky Way, if a CG-SN explodes near the galactic bulge at a Circumgalactic distance less < 3 kpc and a height $z > 1$ kpc where there is virtually no gas, as the blast wave expands in the CGM largely unimpeded, the leading edge pressure discontinuity gradually softens and transitions back to a pressure pulse which diminishes any observable EM wave reflections associated with the difference between the refractive index of the blast wave plasma and the ambient media. In this case the reflection from the blast wave is analogous to a reflection in transmission line, where if an impedance discontinuity occurs along

the transmission path some energy will be reflected and some transmitted in close approximation with the reflection coefficient

$$p_0 = \frac{1}{2}\ln\left({}^{Z_2}/_{Z_1}\right). \quad (2)$$

This equation is applicable to the blast wave where the incident EM wave travels from a media with characteristic impedance Z_1 to a media with characteristic impedance Z_2 with the sign of the result describing the phase of the reflected energy.

Tapering the transmission line at the interface to introduce a more gradual impedance transition is a common technique used to reduce reflections and minimize transmission losses (*50*). In a blast wave propagating with a continuous tapered pressure profile, with the exception of refractive bending it can be shown EM waves will pass transparently through the wave including the condition where the plasma refractive index substantially differs from free space.

3. Plasma Refractive Index

In space, the plasma from a CG-BW has the potential to influence the propagation of light by perturbing the free space refractive index. For plasma, the refractive index η is defined by the relation

$$\eta = \left(1 - \frac{\omega_p^2}{\omega^2}\right)^{1/2} \quad (3)$$

where ω_p is the plasma frequency and ω is the frequency of interest (*1*). Since the plasma frequency is generally measured below 1GHz (*51*) for electron plasmas and lower for ionic plasmas, at light frequencies where $\omega \gg \omega_p$, the plasma refractive index for all practical purposes is equivalent to free space. Based on this equation, the ability of plasmas to influence light propagation, with the exception of ionic resonance, has not previously been considered.

More recent measurements have shown this traditional equation for the plasma refractive index is not valid over a large range of plasma conditions and photon energies. Multiple researchers have reported measuring a plasma refractive index greater than 1 in ionic plasmas using x-ray lasers (*52-55*). The measurements show the electrons bound to ions can dominate the refractive index in many plasmas and drive the index greater than 1. As a result, new average atom code has been developed for calculating the index of refraction in ionic plasmas for photon energies from the optical to soft x-rays (*3*). The new results show for singly ionized plasmas at optical photon energies near a few eV, the refractive index can be substantially greater than the free electron plasma approximation.

The refractive index η for EM radiation can be expressed

$$\eta = \sqrt{\epsilon_r \mu_r} \quad (4)$$

where ϵ_r is the media's relative permittivity and μ_r is the media's relative permeability. While the refractive index measurements on static plasmas discussed previously were driven by the bound electrons increasing the plasma permittivity, high velocity plasmas have additional magnetic properties where permeability becomes a factor. Permeability is a measure of a media's ability to enhance an externally applied magnetic field. Highly permeable media such as iron or nickel-iron composites with μ_r > 20,000 (*56*) are comprised of many magnetic domains, or small regions of aligned magnetic dipoles, which are randomly oriented to minimize the Landau-Lifshitz (*57*) free energy such that the media exhibits minimum magnetization. Two characteristics of highly permeable media are 1) an externally applied magnetic field drives the magnetic domains into alignment increasing the media Landau-Lifshitz free

energy and 2) the resulting increase in media magnetization enhances the applied field. In plasmas traveling at high velocity the charged particles generate a magnetic field. In a manner analogous to a ferromagnetic material increasing magnetism by aligning magnetic dipoles, the high velocity plasma may increase magnetism by aligning the velocity vectors of like charged particles. As such, the permeability of a high velocity plasma is a measure of its ability to align its velocity vectors, in response to an externally applied magnetic field, to increase magnetism to enhance the applied field. Similar to ferromagnetic materials, high permeability requires an initial state with minimum Landau-Lipshitz free energy from which the externally applied field drives the media into a higher state of magnetism. Media starting from an initial highly magnetized state, such as a neodymium magnet with $\mu_r = 1$ (*58*), exhibit low relative permeability. However, high velocity plasmas are known to exhibit diamagnetism ($\mu_r < 1$) when exposed to an external magnetic field (*2*). The external field creates a Lorentz force which drives the moving charged particles into a circular motion constituting a current loop which induces a magnetic flux in opposition to the applied field, resulting in a relative permeability less than one. The magnitude of the induced magnetic flux depends on the density and velocity of the charged particles. To calculate the permeability of a high velocity plasma in the presence of an EM wave, the motion of the individual charged particles must be computed which requires a rigorous solution using Maxwell's equations. Some simplifying assumptions can move the analysis forward and provide an understanding of the underlying forces at work driving the permeability. The EM wave consists of an electric field vector $\boldsymbol{E}$ and a magnetic field vector $\boldsymbol{B}$ which creates a force $\boldsymbol{F}$ on a moving particle of charge q according to the Lorentz equation

$$\boldsymbol{F} = q\boldsymbol{E} + q(\boldsymbol{v} \times \boldsymbol{B}) \tag{5}$$

where $q\boldsymbol{E}$ is the electric force, $q(\boldsymbol{v} \times \boldsymbol{B})$ is the magnetic force and $\boldsymbol{v}$ is the particle velocity vector. To determine the ratio of the electric force to the magnetic force, the characteristic impedance Z_p of the plasma (*59*) is determined based on the equation

$$Z_p = \sqrt{\frac{j\omega\mu_r\mu_0}{\sigma + j\omega\epsilon_r\epsilon_0}} \tag{6}$$

where σ is the plasma conductivity. For very low density plasmas the conductivity is near zero (*60*) which enables the simplification

$$Z_p = \sqrt{\frac{\mu_r\mu_0}{\epsilon_r\epsilon_0}} \tag{7}$$

where $\sqrt{\mu_0/\epsilon_0}$ is the intrinsic impedance of freespace. For an EM wave traveling in a media with characteristic impedance Z_p, the ratio of the electric field E to the magnetic field intensity H is set according to the equation

$$Z_p = \frac{E}{H} \tag{8}$$

and the implied the magnetic field flux density $B = \mu_r\mu_0 H$. While this magnetic flux density includes the cumulative contribution of the magnetic fields from charged particles in the medium through the factor μ_r and is applicable to the EM wave propagation properties, the individual charged particles are separated by relatively large distances and contributions from surrounding charges do not measurably enhance the magnetic flux density in the immediate vicinity of the particle. As a result, the magnetic field

flux density driving the individual particle motion is $B = \mu_0 H$. Substitution yields

$$B = \mu_0 \frac{E}{Z_p} = \mu_0 \sqrt{\frac{\epsilon_r \epsilon_0}{\mu_r \mu_0}} E \qquad (9)$$

and with the speed of light c_p in a plasma with relative permittivity ϵ_r and relative permeability μ_r defined as $c_p = 1/\sqrt{\epsilon_r \epsilon_0 \mu_r \mu_0}$, this expression for magnetic flux density B can be reduced to

$$B = \frac{E}{\mu_r c_p} \qquad (10)$$

where the terms are scaler values. By substitution, the amplitude of the magnetic force on a moving charged particle in the media can be expressed in terms of the electric field as

$$q \frac{v}{\mu_r c_p} E \qquad (11)$$

and when $\mu_r = \epsilon_r = 1$, $c_p =$ C which is the speed of light in vacuum. Since the particle velocity v for CG-BWs will be in the range of 0.03C, the magnetic force will be below the electric force. As the relative permeability μ_r of the medium increases, c_p will decrease with $1/\sqrt{\mu_r}$ which further drives down the magnetic force by the factor $\sqrt{\mu_r}$. As a result, the force on moving charged particles in the media is dominated by the electric force. Looking further at the force vectors, when the EM field travels in the same direction as a parallel component of the particle velocity the electric and magnetic forces are largely in the same direction and the particle motion is consistent with the applied magnetic field which exhibits the previously described diamagnetic properties. However, when the EM field travels the opposite direction of a parallel component of the particle velocity, the electric and magnetic forces are largely in opposite directions and since the electric force dominates, the particle motion follows a path defined by the electric field. This condition is depicted graphically in Fig. 2.

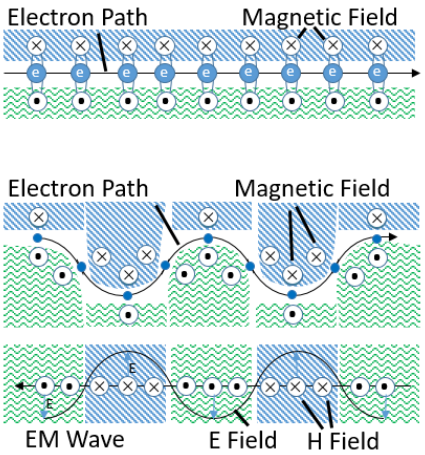

Fig. 2. EM wave influence on an electron magnetic field. At top, free electron traveling left to right generates circular magnetic field lines traveling out of and into the page above and below the electron, respectively. Below, the simulated electron path driven by the EM wave electric field with the electron traveling left to right and the EM wave traveling right to left. As shown, the electron path concentrates its associated magnetic field in phase with the EM wave magnetic field as required to promote paramagnetic properties.

Referencing Fig. 2, the top view shows the magnetic field lines of an electron traveling from left to right across the page. The bottom view shows the electron path under the influence of the electric field of an

EM wave traveling from right to left. The electron particle path increases the magnetic field in-phase with the magnetic field of the EM wave as shown which drives the paramagnetic response. These findings motivate a closer look at the properties of CG-BWs and their applicability to a number of common classes of cosmological observations.

4. CG-BW Pinch Pattern Reflections and Elliptical Galaxies

With the CG-BW traveling radially outward at ~0.025C where C is the speed of light, significant magnetic fields are generated by the high velocity charged particles. Consider a plasma consisting of ions and electrons traveling in parallel away from an observer at high velocity. Ions traveling away will generate a clockwise B-field and electrons traveling away will generate a counterclockwise B-field. An electron traveling under the influence of the ion magnetic field will experience a magnetic force away from the ion and similarly, the electron traveling under the influence of the magnetic field from another electron will experience a magnetic force toward the electron. The magnetic forces in the plasma will tend to segregate the charged particles into cylinders of ions and electrons. This is referred to as the Z-pinch or cylindrical pinch geometry and is known to be sensitive to perturbations destabilizing the static equilibrium of the cylinder (*61*). The magneto-hydrodynamic equilibrium of the cylinders is determined by the balance between kinetic and magnetic pressure with the ratio of pressures referred to as the beta parameter β (*62*)

$$\beta = \frac{2\mu_0 p}{B^2} \qquad (12)$$

where p is the plasma pressure and B is the magnetic field flux density. When $\beta \cong 1$, the magnetic and kinetic pressure forces are nearly in balance. This condition is present at the edge of the cylinder where the plasma pressure must vanish or otherwise align with the ambient pressure outside the cylinder. It can be shown that the plasma pressure in the cylinder as a function of the radial distance r from the center is given by

$$p(r) = p_0 - \frac{B_\phi^2(r)}{2\mu_0} - \frac{1}{\mu_0}\int_0^r \frac{B_\phi^2(\zeta)}{\zeta} d\zeta \qquad (13)$$

where p_0 is the maximum pressure located at the center of the cylinder (*59*). Due to the radial pressure gradient, the plasma toward the center of the cylinder will have a higher density than that at the edge which, as will be discussed later, results in higher luminosity reflections where the plasma pressure pulse encounters a higher density gas and a shock discontinuity forms.

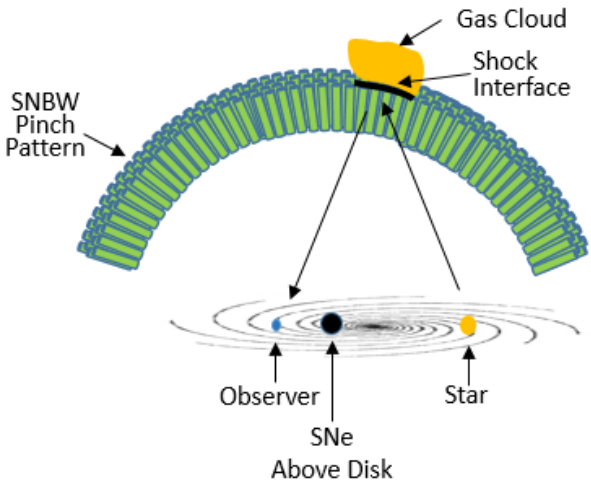

Fig. 3. CG-BW cylindrical pinch pattern reflection. A cross section of the CG-BW pinch pattern is shown shocking a cloud from a superbubble breakout which sets up a pinch patterned reflective shock surface.

Fig. 3 depicts a cross section of a CG-BW where self-generated magnetic fields have driven the plasma into a cylindrical pinch pattern. In regions of space where these pinch patterns encounter higher density clouds, reflections off the CG-BW shock discontinuity would have a luminosity pattern which matches the pinch pattern. With time, as the CG-BW continues to expand and the ambient azimuthal plasma pressure drops, the cylindrical pinch pattern may fade out or self-organize into a more stable pattern with different diameter cylinders. Pinch pattern reflections may be responsible for numerous objects observed in space. Consider elliptical galaxies, the most abundant type galaxy observed in the universe. Elliptical galaxies are believed to be formed from a gas cloud with minimum rotational velocity or through mergers of spiral galaxies (*63-65*). These galaxies can be relatively dim in comparison to spiral galaxies at similar distances and have been observed to range from circular in shape to highly elliptical, where the length is much greater than the width. Many objects classified as elliptical galaxies have an appearance consistent with a slightly out-of-focus star within the Milky Way Galaxy reflecting off the spherical outer surface of a CG-BW as it shocks a slower moving gas cloud as shown in Fig. 3, where the pattern of individual stars within the elliptical galaxy originates from the cylindrical plasma pattern within the CG-BW. Characteristics of elliptical galaxies which are candidates for a CG-BW reflection include a very dim appearance relative to their size and the constituent stars all having a largely identical light spectrum. With this model, the varying length to width ratios of the candidate elliptical galaxies can be explained by spherical aberrations due to off-axis reflections from the CG-BW.

5. Overlapping CG-BWs and Gravitational Lenses

Gravitational lenses are widely observed in the universe and are theoretically formed when light from a distant galaxy passes near to a massive object, such as a foreground galaxy, where the associated gravitational pull bends the path of the light which commonly appears as an arc of light around the object. To further consider how free expanding CG-BWs can appear as a gravitational lens, it is appropriate to first review the plasma properties and environmental conditions impacting the refractive index.

If for a single CG-BW with high radial velocity the ions and electrons segregate into columns as previously discussed, the column relative permeability is expected to be low, as the aligned velocity

vectors generate a high level of magnetism. If the ions and electrons are mixed, the free energy will be lower which increases the relative permeability.

Consider the case of two free expanding CG-BWs originating from two largely separated points in a galaxy, as depicted in Fig. 4A. In the overlapping region, the plasma fields from each CG-BW have similar density and speed but substantially different direction which would disrupt any cylindrical pinch patterns which may have existed previously. A segment of the overlapping region contains a mixture of 4 distinct magnetic alignments established by the ions and electrons traveling in 2 directions, effectively lowering the media free energy below a single CG-BW and further increasing the relative permeability. The angle between the overlapping velocity vectors plays a key role in driving the permeability and determining whether or not a shock discontinuity will form. As discussed previously, the free energy will be at its maximum value when the velocity vectors are in parallel and will transition to its minimum value, which maximizes the permeability, when the vectors are orthogonal. The formation of a shock discontinuity in the overlapping region is dependent on the magnitude of the differential velocity vector. At low acute angles the delta in velocity may not exceed the Alfven and sound speeds of the plasma and a shock condition may not be present. For higher acute angles, whether or not the shock conditions are met, the overlapping region can exhibit more complex behavior such as time dependent rotations of the planes of the magnetic fields which can further lower the free energy and while the nature of such shocks is not fully understood (*66*), the shock discontinuity, if formed in the overlapping region, can be modeled as surfaces at the leading edge of each CG-BW.

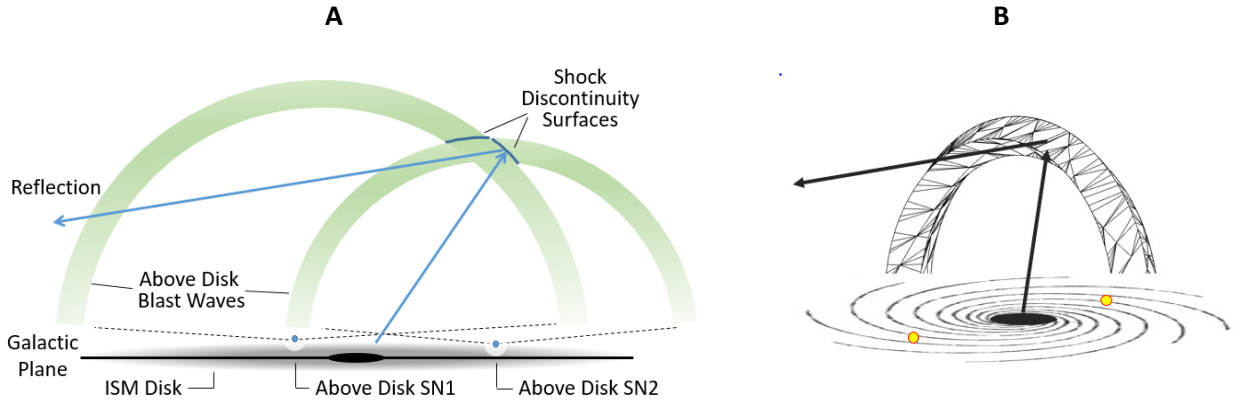

Fig. 4. Intersection of CG-SN Blast Waves. (**A**) Blast waves shown in green from SN1 and SN2 positioned apart in the galaxy intersect and form shock surfaces. Light from the galaxy can reflect off the shock discontinuity in the intersecting region. (**B**) Perspective view of the intersecting blast waves appearing as a partial ring.

The shock surfaces from the overlapping CG-BWs form a semicircle and reflect light from the host galaxy as shown in Fig. 4B and can appear as a gravitational lens. Since the reflecting surfaces are slices from a CG-BW hemisphere, the focal point for an extragalactic distant observer is approximately 1/2 the CG-BW hemisphere radius towards the center and moves as the circular reflective surface is traversed. An arc of reflected light is effectively sourced from different portions of the host galaxy and can highlight the brightness patterns in the underlying spiral pattern.

The light spectrum from gravitational lenses has been studied and found to have an additional redshift with respect to light from the host galaxy (*67,68*), leading to the conclusion that the light originates from a distant receding galaxy. For the light to originate from the host galaxy, the overlapping CG-BWs must introduce the measured redshift. How this redshift occurs is described by first focusing on a single CG-BW. Assume the CG-BW were to expand from an initial width of 0.6 light days, based on 20 days of

ejecta traveling at 0.025C after CSM interaction, to a width of 5k light years over a 2 million year period due to differences in initial particle velocity, changes in particle velocity induced by swept up matter and radial dispersion. Note that the width is the thickness of the blast wave overpressure region, not the diameter of the expanding hemisphere. If linear expansion is assumed for the width, the expansion rate is approximately 0.0025 light years per year which equates to a velocity $v_w = 750$ km s^{-1}. Although not included here, particle interaction in overlapping region is also expected to significantly contribute to the expansion velocity downstream of the leading edge.

To understand how the expansion rate of the width of a CG-BW can induce a redshift, consider the analogous case in Fig. 5 where a wedge is expanding in the light path. Initially an observer and remote light source are stationary in a medium with refractive index $\eta_0 = 1$ and no Doppler or redshift is present in the light received from the remote source.

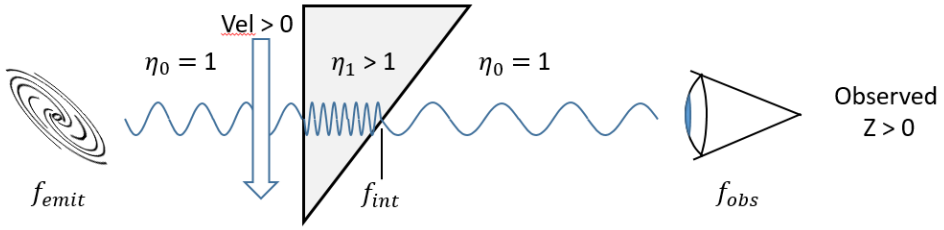

Fig. 5. Redshift *z* induced between stationary end points during refractive index change. Refractive index of the propagation path is increasing as the wedge ($\eta_1 > 1$) is expanding in the line of sight. With the wedge moving as shown the redshift present at the wedge interface receding from the emitter exceeds the blueshift from the wedge interface approaching the observer resulting in a net redshift along the observation path.

The wedge in Fig. 5 with refractive index $\eta_1 > 1$ is then moved through the light path as shown with velocity v in m s^{-1} for a period of time T. During T, the wedge is displacing media with refractive index $\eta_0 = 1$ in the observation path with media with refractive index $\eta_1 > 1$. The velocity v_w at which the dielectric wedge width is growing in the observation path is

$$v_w = v * TAN\ \alpha \qquad (14)$$

where α is the angle of the wedge leading edge. The net shift in the emission frequency f_{emit} can be determined by first calculating the frequency at the wedge interface f_{int} shown in Fig. 5 as it expands along the observation path. The frequency f_{int} with respect to f_{emit} is given by

$$f_{int} = \left(\frac{c/\eta_1 - v_w}{c/\eta_1}\right) f_{emit} \qquad (15)$$

where c/η_1 is the speed of light in the wedge. Note for positive v_w the frequency is redshifted as the interface is receding from the source frequency at the wedge input. The frequency observed f_{obs} with respect to f_{int} is given by

$$f_{obs} = \left(\frac{c/\eta_0}{c/\eta_0 - v_w}\right) f_{int} \qquad (16)$$

where c/η_0 is the speed of light in free space. For positive v_w the frequency observed is blueshifted as the wedge interface is moving toward the observer. Substituting for f_{int} and simplifying provides the relationship between f_{obs} and f_{emit} as

$$f_{obs} = \left(\frac{c - v_w\eta_1}{c - v_w\eta_0}\right) f_{emit.} \qquad (17)$$

Based on this equation, when $v_w > 0$ and $\eta_1 > \eta_0$ a net redshift will be present along the observation path. This redshift induced by a change in the refractive index along the light path may be incorrectly attributed to Doppler. When the wedge stops moving with $v_w = 0$ the redshift returns to zero. Moving the wedge laterally along the observation path does not store additional cycles in this example as the light path through the wedge does not increase. Note that It is possible to set η_1 such that $f_{obs} < 0$. In this case the wedge expansion velocity v_w is greater than the speed of light $^{c}/_{\eta_1}$ in the wedge, in which case light does not exit the wedge. Under these conditions f_{obs} = 0.

To further analyze the overlapping CG-BW case, consider a hypothetical example where a host galaxy is observed with a redshift $z = 3$ and the reflection from an overlapping CG-BW is observed with a redshift $z = 4$ which implies the reflected light has been redshifted by $z = 1$ relative to the host galaxy. Assuming the CG-BW redshift $z = 1$ was based on a shift of the Hα line at an approximate rest wavelength of 656.3 nm or frequency of 4.57 x 10^{14} Hz, the refractive index of the overlapping CG-BWs may be calculated. The redshift z is defined as

$$z = \frac{f_{emit} - f_{obs}}{f_{obs}} \tag{18}$$

where f_{emit} is the source frequency and f_{obs} is the observed frequency. Then

$$\frac{f_{obs}}{f_{emit}} = \frac{1}{z+1} \tag{19}$$

and from equation 17 with η_0 set to 1

$$\frac{f_{obs}}{f_{emit}} = \left(\frac{c - v_w\eta_1}{c - v_w}\right). \tag{20}$$

Solving equations 19 an 20 for η_1 yields

$$\eta_1 = \frac{c(z+1) - (c - v_w)}{v_w(z+1)}. \tag{21}$$

Substituting $z = 1$, $v_w =$ 750 km s^{-1} and $c =$ 3 x 10^8 m s^{-1} into equation 21 yields $\eta_1 = 201$. From equation 4, the relative permittivity and permeability are related to the index of refraction by

$$\eta = \sqrt{\epsilon_r \mu_r}\,.$$

If we assume the relative permittivity ϵ_r driven by the bound electrons is slightly larger than 1 with a value of 1.5, the relative permeability for the overlapping CG-BW is calculated as

$$\mu_r = \frac{\eta_1^2}{\epsilon_r} = 26{,}934\,. \tag{22}$$

This relative permeability is in the range of some iron-based materials, which have been measured at 20,000 and higher (*56*). The relative permeability calculated above is largely a function of the expansion velocity v_w. For example, if particle interaction causes an increase in the overlapping region expansion velocity to 2,000 km s^{-1}, the relative permeability would drop to 3,866.

To recap, for EM waves traveling opposite the overlapping CG-BW particle velocity, the plasma characteristic impedance impacts the permeability by 1) driving up the EM wave electric field responsible for the particle motion which increases the plasma magnetization and 2) driving down the EM wave magnetic field H which then further increases the permeability by the relationship B/H. As the magnetic field generated by the plasma increases with velocity, the permeability will also increase with velocity. In

a plasma of electrons and ions, the permeability will be driven by the electrons since the electron mass is $< 1/1000$ of the ion mass resulting in the electron path being more strongly influenced by the applied electric field. As the paramagnetic properties come about from electric forces changing the path of free electrons, depending on the electron velocity the paramagnetic behavior can be observed over a wide band of EM wavelengths, including most ranges used in celestial observations. As a result, light reflected from the intersecting CG-BWs will be achromatically redshifted. This brief qualitative analysis demonstrates conditions under which a high velocity plasma exhibits paramagnetic properties and supports the supposition the gravitational lens' redshift relative to the host galaxy is induced by the refractive index of the expanding, intersecting CG-BWs.

Many observed gravitational lenses exhibit choppiness along the arc, which is expected where sections of the CG-BW hemispherical surface previously encountered clouds during the free expansion.

In rare cases strong gravitational lensing can produce quadruple images of a lensed quasi-stellar object (QSO) which have been observed in the form of an Einstein Cross. One theory of how these structures form is from small scale dark matter structures positioned along the light path (*69*). These rare Einstein Cross structures can also be formed from 4 intersecting CG-BWs where the quadruple image is comprised of reflected light from the central galaxy.

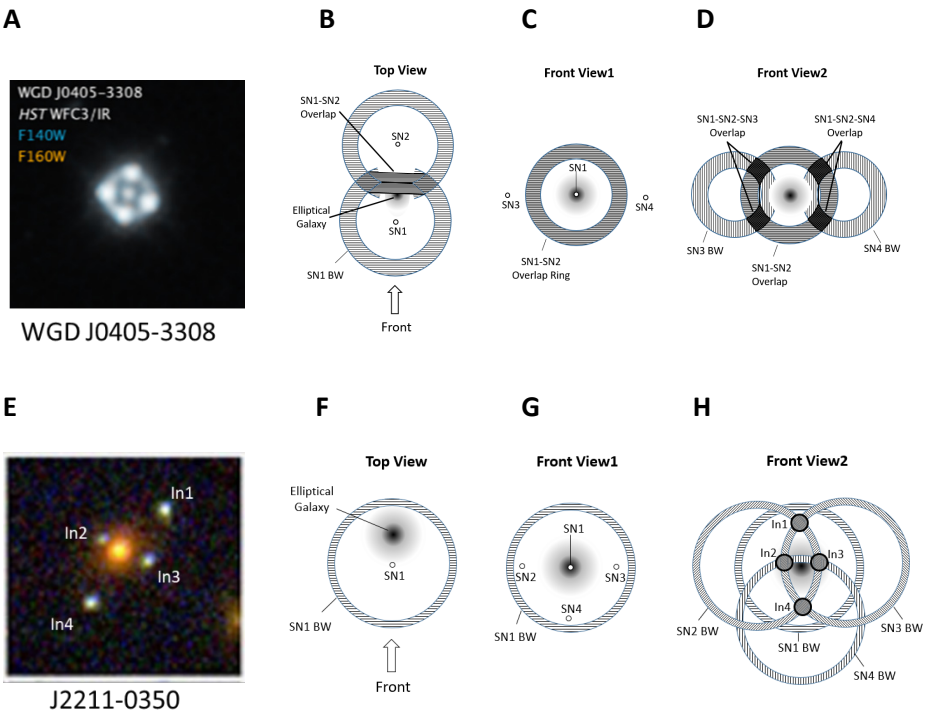

Fig. 6. Einstein Cross images and underlying CG-BWs. (**A**) Image of Einstein Cross WGD J0405-3308. **(B&C)** Top and front view of intersection ring formed from SN1 and SN2. **(D)** Triple intersections of blast waves SN1-SN4 forming the Einstein Cross pattern in dark grey. **(E)** Image J2211-0350 with Einstein Cross. **(F&G)** Top and front view of SN1 blast wave. **(H)** Triple intersections of blast waves forming the Einstein Cross pattern points In1-In4.

Fig 6A is a Hubble Space Telescope image of Einstein Cross WGD-J0405-3308 which is considered the front view orientation in the following descriptions. Fig. 6B is a top view of the structure with two of the

four SN blast waves shown with a horizontal hash pattern positioned in front of and behind the central elliptical galaxy. The SNs are distanced from the central galaxy such that only an approximate 30 degree sector of the blast waves are substantially absorbed and blocked by the galaxy. The overlap of the SN1 and SN2 blast waves form a ring which can be seen in the front view of Fig. 6C, along with the positions of SN3 and SN4. In Fig. 6D, the blast waves from SN3 and SN4 are shown in vertical crosshatch. The intersection of the ring from SN1 and SN2 with the spherical blast waves from SN3 and SN4 form 4 shocked overlapping regions as shown with triple the plasma density of a single blast wave, which creates the bright reflections at the Einstein Cross points. Note that the rectangular cross section of the dark shaded triple overlap regions in Fig. 6D are partially visible in the Fig. 6A image. Fig. 6E is a Hubble Space Telescope image of an Einstein Cross configuration discovered by close inspection of an image of galaxy cluster J2211-0350 (*70*). Fig. 6F is a top view of the structure which includes the central elliptical galaxy and the position of SN1 and its associated blast wave. Fig. 6G is a front view which includes the positions of SN2, SN3 and SN4 around the galaxy. In Fig. 6H, the blast waves of SN2, SN3 and SN4 are added. The blast waves from SN2 and SN3 intersect to form an overlap ring. This ring intersects the spherical blast wave from SN1 at the far side of the elliptical galaxy at intersection points In1 and In4. Similarly, the blast waves from SN2 and SN4 and the blast waves from SN3 and SN4 form rings which intersect with SN1's blast wave at points In3 and In2, respectively. The intersections In1 to In4 are each comprised of 3 blast waves with triple the plasma density of a single blast wave, driving bright reflections from the outer shocked surface of SN1's blast wave which forms the Einstein Cross points.

Gravitational lenses have been observed around galaxy clusters, where the summation of the cluster mass creates a gravitational field which bends the light of a distant galaxy. One example of a galaxy cluster lens is the "Sunburst Arc" observed with the Hubble Telescope (*71*). Analysis of large circular arcs formed near galaxy clusters indicate the Einstein radii determined by the cluster mass density versus the area enclosed by the arc can differ by 10-30% (*72*). Measurements of gravitational microlensing of near-field objects, such as a foreground star crossing in front of a background star, experience similar uncertainties as present imaging limitations do not allow accurate resolution of the lens from the source at the time of the event (*73*). Since intergalactic SN have been observed in galaxy clusters (74), it is feasible that the associated blast waves freely expanding in a very low density IGM can reach the radii of the observed cluster arcs and overlapping blast waves can produce gravitational lens structures equivalent to the "Sunburst Arc".

6. Plasma Saturation and the Hubble Constant

Cold gases, such as Bose Einstein Condensates, have been shown to dramatically slow the propagation of light under resonant frequency conditions (*75,76*). In further work, measurements of these cold gases indicate the refractive index exhibits a saturation phenomenon analogous to magnetic saturation in a paramagnetic material without hysteresis. Multiple reports indicate the velocity of light pulses through Bose Einstein Condensates vary with the intensity of the coupling beam and in fact can be controlled with the beam power (*77,78*). Experiments on the group velocity temperature dependency in cold gas have shown the variation of the spatial density of atoms with temperature is the major factor driving the increase in group velocity versus temperature (*79*). Although to be confirmed with measurements, the reported data supports the hypothesis that even for off-resonant frequencies a direct correlation exists between the gas density and the plasma saturation point, where the plasma saturation point is defined as the maximum light intensity before the group delay increases. As described graphically in Fig. 7, for a region of plasma at fixed temperature and with uniform density, a saturation limit is applicable for a light source impinging on the plasma which defines the maximum number of simultaneous photons the plasma

can engage, where photons above the maximum limit transparently pass through the plasma. As the plasma density increases, the saturation limit increases. In a behavior similar to resonant cold gases, when multiple light sources impinge on plasma from multiple directions, the plasma saturation curve is expected to shift down with increased cumulative source power while the resulting saturation limit remains applicable for each independent light source.

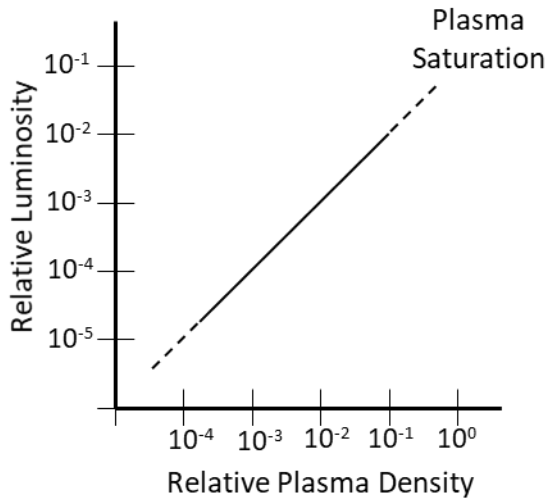

Fig. 7. Plasma saturation as a function of plasma density and luminosity. For light passing through the plasma at luminosity above the saturation point, the plasma is transparent.

Fig. 7 implies the plasma can influence photons at orders of magnitude below what may be considered optically thin plasma densities. Considering the photon as a wave, as opposed to a particle, a single photon approaching an observatory as a plane wave may have its propagation influenced by charged particles encountered tens of thousands of light years away which may be distributed over a surface area of a few square light years or more. With light propagation through cosmological distances, describing plasma saturation density in terms of particles contained within an effective aperture or column density may be more appropriate. At the limit, a single ion encountered by the plane wave surface traveling in the column could capture and briefly delay the photon.

Application of these plasma saturation properties to the CG-BWs expanding in the galaxy can emulate the Hubble Law

$$H_0 = {}^{v_r}/_{d} \qquad (23)$$

where H_0 is the Hubble constant, v_r is the recession velocity and d is the distance to an observed galaxy. Ongoing measurements of the Hubble constant using different distance estimation techniques have not been able to converge on a single value (*80,81*). The convergence problem is primarily related to the difficulty in establishing an accurate distance to an observed object over large cosmological scales. Numerous methods are used for distance estimation including Type Ia SN, which relies on known SN luminosity, the Tully-Fisher Relation (TFR), which for late-type galaxies relies on a measurement of the galaxy's rotational velocity to infer the intrinsic luminosity, and the Cepheid star which relies on measurement of the Cepheid period to estimate the star's luminosity (*82*). For each method, the objects inferred luminosity is used in conjunction with the observed luminosity to estimate the distance. Of these techniques, only the measurement of the Cepheid period is subject to change due to redshift. In this case,

the increase in Cepheid period from recession due to an expanding universe would appear identical had the recession occurred while refractive index of the intervening media was increasing. Hence the distance measurement techniques are expected to be independent of the mechanism inducing the recession velocity.

CG-BWs can be modeled to closely emulate the Hubble constant. If the SN rate over the last 2 million years was consistent with modeled observability (*32*) and assuming <1 in 1000 SN occur outside the ISM and generate CG-BWs, a sphere encompassing the galaxy may be filled with regions of vacuum, single CG-BWs and overlapping CG-BWs having for this example indices of refraction of 1, >1 and >>1, respectively. Light passing through the galactic sphere will encounter multiple expanding CG-BWs and, where the light luminosity is below the CG-BW plasma saturation point, each CG-BW will introduce an incremental redshift. This scenario is depicted graphically in Fig. 8, where an exemplary plot of CG-BW plasma density versus distance to the galactic plane has been generated for a ~4M year history of CG-BW events, with each event shaded in blue or green.

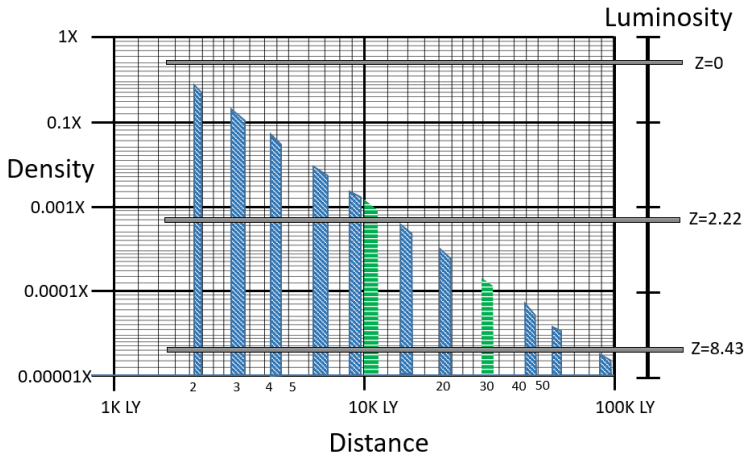

Fig. 8. Impact of CG-SN history on observed redshift. Example CG-BW history encountered by an extragalactic light source traveling to a point within the galaxy. Graph depicts CG-BW column density versus distance in light years with common radial and width expansion rates, where blue bars represent individual CG-BWs (z = 0.1) and green bars represent overlapping CG-BWs (z = 1.0). The light source luminosity impacts which CG-BWs influence the observed redshift z as luminosity above the CG-BW saturation point passes through transparently, as shown in 3 luminosity level examples.

The blue diagonally hatched events depict single CG-BWs which induce a redshift of $z = 0.1$ and the green horizontally hatched events depict overlapping CG-BWs which induce a redshift of $z = 1.0$. On the right of Fig. 8 is a scale of luminosity which shows how the redshift of the light is influenced at 3 different luminosity levels. At higher levels of luminosity, the light is above the plasma saturation level and passes through the CG-BWs without a redshift. At mid luminosity levels, the light is above the saturation levels of the CG-BWs farther out than ~15k light years but is below the saturation levels of the more dense plasmas from closer in CG-BWs which introduce sequentially redshifts, where this example includes 1 overlapping CG-BW of $z = 1$ and 5 single CG-BWs of $z = 0.1$ for a total cascaded redshift of $z = 2.22$. At very low luminosity levels the light is below the saturation level of many older and farther out CG-BWs which incrementally add to the cascaded redshift totaling $z = 8.43$ in this case. With a SN event rate closer to the modeled observability, the discrete example here could be replaced by a continuum of overlapping CG-BWs, where the galactic sphere would be filled with regions of plasma with varying refractive indices, based on the amount of CG-BW overlap. In general, the high refractive

index plasma regions would expand as the underlying independent CG-BWs expand. The varying refractive index regions would be expected to follow a similar luminosity redshift relationship as shown in the example in Fig. 8.

7. Summary

In summary, the measurements and analysis presented collectively demonstrate space plasmas, traditionally thought to be transparent, can exhibit EM properties with significant potential to influence cosmological observations. When these plasma properties are applied to CG-SN blast wave models, the dynamic physical geometry of the plasma fields create reflections and redshifts which can accurately align with multiple classes of cosmic observations including elliptic galaxies, gravitational lenses and the Hubble constant. Aside from reflections off shock discontinuities, direct evidence of freely expanding CG-BWs is predictably difficult to find in the large body of observational data on the Milky Way due to 1) the low rate of occurrence reduces early phase detections, 2) the plasmas rapidly cool, are optically thin and non-emissive, 3) the propagation medium is too thin to generate a detectable radio emission and 4) the plasma density is too low for detection by absorption spectroscopy. The large body of observational data on galactic halos and CGMs do not rule out CG-BWs and has been shown to provide indirect evidence lending support to their existence. The intersecting CG-BW model is better aligned with the observational data for gravitational lenses than the existing light bending theory in which significant inconsistencies remain unresolved. Einstein Cross gravitational lens observations provide strong direct evidence supporting the CG-BW models as these lens configurations cannot be reasonably explained by the light bending theory. Other categories of observations which may be related to CG-BWs include globular clusters, ghost or ultra-diffuse galaxies (*83*) and the Lyman-Alpha forest (*84*). The CG-BW theory relies on high velocity plasmas exhibiting conditional paramagnetic properties, as supported by the analysis. Construction of an appropriate laboratory apparatus which creates a region of intersecting high velocity electron beams with controllable density could be used to measure the EM wave permeability to validate the plasma behavior derived in the analysis.

Conflicts of Interest: The author declares no conflict of interest.

References:

1. U. S. Inan, M. Golkowski, "Introduction to waves in plasmas" in *Principles of Plasma Physics for Engineers and Scientists* (Cambridge Univ. Press, 2011).
2. D. A. Gurnett, A. Bhattacharjee, "Single particle motions" in *Introduction to Plasma Physics* (Cambridge Univ. Press, 2017).
3. J. Nilsen, W. R. Johnson, *Analysing the dramatic impact of the bound electron contribution to the index of refraction in plasmas*, (2004).
4. D. Branch, J. C. Wheeler, *Supernova Explosions* (Springer, 2017).
5. E. O. Ofek, I. Arcavi, D. Tal, M. Sullivan, A. Gal-Yam, S. R. Kulkarni, P. E. Nugent, S. Ben-Ami, D. Bersier, Y. Cao, S. B. Cenko, A. De Cia, A. V. Filippenko, C. Fransson, M. M. Kasliwal, R. Laher, J. Surface, R. Quimby, O. Yaron, Interaction-powered supernovae: rise-time vs. peak-luminosity correlation and the shock-breakout velocity. *Ap. J.* **788**, 154 (2014).
6. D. Branch, M. Livio, L. R. Yungelson, F. R. Boffi, E. Baron, In search of the progenitors of Type Ia supernovae. *Pub. A.S. Pac.* **107**, 1019-1029 (1995).
7. A. V. Filippenko, Optical spectra of supernovae. *A.R. A.&A.* **35**, 309-55 (1997).
8. W. Hillebrandt, J. C. Niemeyer, Type Ia supernova explosion models. *A.R. A.&A.* **38**, 191-230 (2000).
9. P. Hoflick, A. Khokhlov, Explosion models for Type Ia supernovae: a comparison with observed light curves, distances, H_0, and q_0. *Ap. J.* **457**, 500-528 (1996).
10. S. Haid, S. Walch, T. Naab, D. Seifried, J. Mackey, A. Gatto, Supernova-blast waves in wind-blown bubbles, turbulent, and power-law ambient media. *MNRAS* **460**, 2962-2978 (2016).
11. F. G. Freidlander, The diffraction of sound pulses I. Diffraction by a semi-infinite plane. *Proc. Roy. Soc. Lond. A* **186**, 322-344 (1946).
12. D. A. Gurnett, A. Bhattacharjee, "Discontinuities and Shock Waves" in *Introduction to Plasma Physics* (Cambridge Univ. Press, 2017).
13. B. W. Keller, J. Wadsley, H. M. P. Couchman, Cosmological galaxy evolution with superbubble feedback – I. Realistic galaxies with moderate feedback. *MNRAS* **453**, 3499-3509 (2015).
14. V. Springel, L. Hernquist, Cosmological smoothed particle hydrodynamics simulations: a hybrid multiphase model for star formation. *MNRAS* **339**, 289-311 (2003).

15. G. Stinson, A. Seth, N. Katz, J. Wadsley, F. Governato, T. Quinn, Star formation and feedback in smoothed particle hydrodynamic simulations – I. Isolated galaxies. *MNRAS* **373**, 1074-1090 (2006).
16. M. Li, G. L. Bryan, J. P. Ostriker, Quantifying supernovae-driven multiphase galactic outflows. *Ap. J.* **841**, 101-116 (2017).
17. C. Heiles, Clustered supernovae versus the gaseous disk and halo. *Ap. J.* **354**, 483-491 (1990).
18. C-G. Kim, E. C. Ostriker, R. Raileanu, Superbubbles in the multiphase ISM and the loading of galactic winds. *Ap. J.* **834**, 25 (2017).
19. A Camps-Farina, J. Zaragoza-Cardiel, J. E. Beckman, J. Font, P. F. Valazquez, A. Rodriguez, M. Rosado, Physical properties of superbubbles in the Antennae galaxies. *MNRAS* **468**, 4134-4142 (2017)
20. B. T. Draine, *Physics of the Interstellar and Intergalactic Medium* (Princeton University Press, 2011).
21. G. Courtes, H. Petit, J.-P. Sivan, S. Dodonov, M. Petit, Hα survey of M33 with the six-meter telescope: Morphology of the general diffuse emission, evidence for a chaotic medium of bubbles and filaments. *A.&A.* **174**, 28-56 (1987).
22. S. Diel, T. S. Statler, The hot interstellar medium of normal elliptical galaxies. II. Morphological evidence for active galactic nucleus feedback. *Ap. J.* **680**, 897-910 (2008).
23. S. Malhotra, D. Hollenbach, G. Helou, N. Silbermann, E. Valjavec, R. H. Rubin, D. Dale, D. Hunter, N. Lu, S. Lord, H. Dinerstein, H. Thronson, Probing the interstellar medium in early-type galaxies with Infrared Space Observatory observations. *Ap. J.* **543**, 634-643 (2000).
24. M. T. Sargent, E. Daddi, F. Bournaud, M. Onodera, C. Feruglio, M. Martig, R. Gobat, H. Dannerbauer, E. Schinnerer, A direct constraint on the gas content of a massive, passively evolving elliptical galaxy at z = 1.43. *Ap. J. Lett.* **806**, L20 (2015).
25. G. A. Welch, L. J. Sage, The interstellar medium of M32. *Ap. J.* **557**, 671-680 (2000).
26. J. Maza, S. van den Bergh, Statistics of extragalactic supernova. *Ap. J.* **204**, 519-529 (1976).
27. D. J. Patnaude, C. Badenes, S. Park, J. M. Laming, The origin of Kepler's supernova remnant. *Ap. J.* **756**, 6 (2012).
28. I. J. Danziger, W. M. Goss, The distance of Kepler's supernova remnant. *MNRAS* **190**, 47-49 (1980).
29. S. van den Bergh, A. P. Marscher, Y. Terzian, An optical atlas of galactic supernova remnants. *Ap. J. S.S.* **26**, 19-36 (1973).
30. S. P. Reynolds, K. J. Borkowski, U. Hwang, J. P. Hughes, C. Badenes, J. M. Laming, J. M. Blondin, A deep Chandra observation of Kepler's supernova remnant: A Type Ia event with circumstellar interaction. *Ap. J.* **668**, L135-L138 (2007).
31. C. F. McKee, J. P. Ostriker, A theory of the interstellar medium: Three components regulated by supernova explosions in an inhomogeneous substrate. *Ap. J.* **218**, 148-169 (1977).
32. S. M. Adams, C. S. Kochanek, J. F. Beacom, M. R. Vagins, K. Z. Stanek, Observing the next galactic supernova. *Ap. J.* **778**, 164-179 (2013).
33. K. L. Adelberger, C. C. Steidel, A. E. Shapley, M. Pettini, Galaxies and intergalactic matter at redshift z ~ 3: Overview. *Ap. J.* **584**, 45-75 (2003).
34. A. Aguirre, L. Hernquist, J. Schaye, D. H. Weinberg, N. Katz, J. Gardner, Metal enrichment of the intergalactic medium at z = 3 by galactic winds. *Ap. J.* **560**, 599-605 (2001).
35. J. M. Shull, Where do galaxies end?, *Ap. J.* **784**, 142 (2014).
36. J. X. Prochaska, J. K. Werk, G. Worseck, T. M. Tripp, J. Tumlinson, J. N. Burchett, A. J. Fox, M. Fumagalli, N. Lehner, M. S. Peeples, N. Tejos, The COS-Halos Survey: Metallicities in the low-redshift circumgalactic medium. *Ap. J.* **837**, 169 (2017).
37. T. M. Heckman, Starburst-driven galactic winds. *Rev. Mex. AA* **17**, 47-55 (2003).
38. M. S. Peeples, F. Shankar, Constraints on star formation driven galaxy winds from the mass-metallicity relation at z = 0. *MNRAS* **417**, 2962-2981 (2011).
39. D. K. Strickland, T. M. Heckman, Supernova feedback efficiency and mass loading in the starburst and galactic superwind exemplar M82. *Ap. J.* **697**, 2030-2056 (2009).
40. B. D. Savage, K. R. Sembach,B. P. Wakker, P. Richter, M. Meade, E. B. Jenkins, J. M. Shull, H. W. Moos, G. Sonneborn, Distribution and kinematics of O VI in the galactic halo. *Ap. J.* **146**, 125-164 (2003).
41. J. Roman-Duval, M. Heyer, C. M. Brunt, P. Clark, R. Klessen, R. Shetty, Distribution and mass of diffuse and dense CO gas in the Milky Way. *Ap. J.* **818**, 144 (2016).
42. R. Ganguly, K. Sembach, T.M. Tripp, B. D. Savage, Highly ionized gas in the galactic halo and the high-velocity clouds toward PG 1116+215. *Ap. J.S.S.* **157**, 251-278 (2005).
43. K. R. Sembach, B. P. Wakker, B. D. Savage, P. Richter, M. Meade, J. M. Shull, E. B. Jenkins, G. Sonneborn, H. W. Moos, Highly ionized high-velocity gas in the vicinity of the galaxy. *Ap. J.S.S.* **146**, 165-208 (2003).
44. J. A. Gritton, R. L. Shelton, K. Kwak, Mixing between high velocity clouds and the galactic halo. *Ap. J.* **795**, 99 (2014).
45. E. Shulman, J. N. Bregman, M. S. Roberts, An H I survey of high-velocity clouds in nearby disk galaxies. *Ap. J.* **423**, 180-189 (1994).
46. F. J. Lockman, The H I halo in the inner galaxy. *Ap. J.* **283**, 90-97 (1984).
47. E. Hummel, R. Beck, R.-J. Dettmar, An Effelsberg/VLA radio continuum survey of an optically selected sample of edge-on spiral galaxies. *A&A S.S.* **87**, 309-317 (1991).
48. C. Heiles, H I shells and supershells. *Ap. J.* **229**, 533-544 (1979).
49. C. Heiles, H I shells, supershells, shell-like objects, and "worms". *Ap. J. S.S.* **55**, 585-595 (1984).
50. R. W. Klopfenstein, A transmission line taper of improved design. *Proc. I.R.E.* **1**, 31-35 (1956).
51. L. Tonks, I. Langmuir, Oscillations in ionized gases. *Phys. Rev.* **33**, 195-211 (1929).
52. J. Filevich, J. Grava, M. Purvis, M. C. Marconi, J. J. Rocca, J. Nilsen, J. Dunn, W. R. Johnson, Multiply ionized carbon plasmas with an index of refraction greater than one. *Laser and Particle Beams* **25**, 47-51 (2007).
53. J. Nilsen, J. H. Scofield, Plasmas with an index of refraction greater than 1. *Opt. Lett.* **29**, 2677-2679 (2004).
54. J. Nilsen, W. R. Johnson, Plasma interferometry and how the bound-electron contribution can bend fringes in unexpected ways. *Ap. Opt.* **44**, 7295-7301 (2005).

55. J. Filevich, J. J. Rocca, M. C. Marconi, S. J. Moon, J. Nilsen, J. H. Scofield, J. Dunn, R. F. Smith, R. Keenan, J. R. Hunter, V. N. Shlyaptsev, Observation of a multiply ionized plasma with an index of refraction greater than one. *Phys. Rev. Lett.* **94**, 035005 (2005).
56. John R. Rumble, *Handbook of Chemistry and Physics*, (2019).
57. B. D. Cullity, C. D. Graham, *Introduction to Magnetic Materials*, (2009).
58. D. Jiles, "Magnetic Materials" in *Introduction to Magnetism and Magnetic Materials* (CRC Press, 2016).
59. W. H. Hayt, "The Uniform Plane Wave" in *Engineering Electromagnetics* (McGraw-Hill, 1974).
60. U. S. Inan, M. Golkowski, "Collisions and plasma conductivity" in *Principles of Plasma Physics for Engineers and Scientists* (Cambridge Univ. Press, 2011).
61. D. A. Gurnett, A. Bhattacharjee, "MHD equilibria and stability" in *Introduction to Plasma Physics* (Cambridge Univ. Press, 2017).
62. U. S. Inan, M. Golkowski, "Single-fluid theory of plasmas: magnetohydrodynamics" in *Principles of Plasma Physics for Engineers and Scientists* (Cambridge Univ. Press, 2011).
63. G. Zhu, M. R. Blanton, J. Moustakas, Stellar populations of elliptical galaxies in the local universe. , *Ap. J.* **722**, 491-519 (2010).
64. R. P. van der Marel, P. G. van Dokkum, Dynamical models of elliptical galaxies in z = 0.5 clusters. I. Data-model comparison and evolution of galaxy rotation. *Ap. J.* **668**, 738-755 (2007).
65. T. Naab, J. P. Ostriker, Are disk galaxies the progenitors of giant ellipticals?. *Ap. J.* **690**, 1452-1462 (2009).
66. B. T. Draine, C. F. McKee, Theory of interstellar shocks. *A.R. A.&A.* **31**, 373-432 (1993).
67. E. O. Ofek, H.-W. Rix, D. Maoz, The redshift distribution of gravitational lenses revisited: constraints on galaxy mass evolution, *MNRAS* **343**, 639–652 (2003).
68. M Fukugita, T. Futamase, M. Kasai, E. L. Turner, Statistical properties of gravitational lenses with a nonzero cosmological constant. *Ap. J.* **393**, 3-21 (1992).
69. A. M. Nierenberg, D. Gilman, T. Treu, G. Brammer, S. Birrer, L. Moustakas, A. Agnello, T. Anguita, C. D. Fassnacht, V. Motta, A. H. G. Peter, D. Sluse, Double dark matter vision: twice the number of compact-source lenses with narrow-line lensing and the WFC3 grism. *MNRAS* **492**, 5314-5335 (2019).
70. D. Bettoni, R. Falomo, R. Scarpa, M. Nagrello, A. Omizzolo, R. L. M. Corradi, D. Raverte, B. Vulcani, A new Einstein Cross gravitational lens of a Lyman-break galaxy. *Ap. J. Lett.* **873**, L14 (2019).
71. T. E. Rivera-Thorsen, H. Dahle, J. Chisholm, M. K. Florian, M. Gronke, J. R. Rigby, M. D. Gladders, G. Mahler, K. Sharon, M. Bayliss, Gravitational lensing reveals ionizing ultraviolet photons escaping from a distant galaxy. *Sci.* **366**, 738-741 (2019).
72. E. Puchwein, S. Hilbert, Cluster strong lensing in the Millennium simulation: the effect of galaxies and structures along the line-of-sight. *MNRAS* **398**, 1298-1308 (2009).
73. C. B. Henderson, H. Park, T. Sumi, A. Udalski, A. Gould, Y. Tsapras, C. Han, B. S. Gaudi, V. Bozza, F. Abe, D. P. Bennett, I. A. Bond, C. S. Botzler, M. Freeman, A. Fukui, D. Fukunaga, Y. Itow, N. Koshimoto, C. H. Ling, K. Masuda, Y. Matsubara, Y. Muraki, S. Namba, K. Ohnishi, N. J. Rattenbury, T. Saito, D. J. Sullivan, D. Suzuki, W. L. Sweatman, P. J. Tristram, N. Tsurumi, K. Wada, N. Yamai, P. C. M. Yock, A. Yonehara, M. K. Szymanski, M. Kubiak, G. Pietrzynski, I. Soszynski, J. Snowron, S. Kozlowski, R. Poleski, K. Ulaczyk, L. Wyrzykowski, P. Pietrukowicz, L. A. Almeida, M. Bos, J.-Y. Choi, G. W. Christie, D. L. Depoy, S. Dong, M. Freidmann, K.-H. Hwang, F. Jablonski, Y. K. Jung, S. Kaspi, C.-U. Lee, D. Maoz, J. McCormick, D. Moorehouse, T. Natusch, H. Ngan, R. W. Pogge, I.-G. Shin, Y. Shvartzvald, T.-G. Tan, G. Thornley, J. C. Yee, A. Allan, D. M. Bramich, P. Browne, M. Dominik, K. Horne, M. Hundertmark, R. Figuera Jaimes, N. Kains, C. Snodgrass, I. A. Steele, R. A. Street, Candidate gravitational microlensing events for future direct lens imaging. *Ap. J.* **794**, 71 (2014).
74. D. Maoz, E. Waxman, A. Loeb, The remnants of intergalactic supernova. *Ap. J.* **632**, 847-853 (2005).
75. L. V. Hau, S. E. Harris, Z. Dutton, C. H. Behroozi, Observation of quantum shock waves created with ultra-compressed slow light pulses in a Bose-Einstein condensate. *Nat.* **397**,594-598 (1999).
76. S. Baier, M. J. Mark, D. Petter, K. Aikawa, L. Chomaz, Z. Cai, M. Baranov, P. Zoller, F. Ferlaino, Extended Bose-Hubbard models with ultracold magnetic atoms. *Sci.* **352**, 201-205 (2016).
77. C. Slowe, N. S. Ginsberg, T. Ristroph, A. Goodsell, L. V. Hau, Ultraslow light & Bose-Einstein condensates. *Opt. & Phot. News* **16**, 30-34 (2005).
78. M. J. Akram, F. Ghafoor, M. M. Khan, F. Saif, Control of Fano resonances and slow light using Bose-Einstein condensates in a nanocavity. *Phys. Rev. A* **95**, 023810 (2017).
79. G. Morigi, G. S. Agarwal, Temperature variation of ultraslow light in a cold gas. *QELS 2000*, QtuA28 (2000).
80. W. L. Freedman, B. F. Madore, B. K. Gibson, L. Ferrarese, D. D. Kelson, S. Sakai, J. R. Mould, R. C. Kennicutt, Jr., H. C. Ford, J. A. Graham, J. P. Huchra, S. M. G. Hughes, G. D. Illingworth, L. M. Macri, P. B. Stetson, Final results from the Hubble Space Telescope key project to measure the Hubble constant. *Ap. J.* **553**, 47-72 (2001).
81. X-P. Wu, Z. Deng, Z. Zou, L.-Z. Fang, B. Qin, On the measurement of the Hubble Constant in a local low-density universe. *Ap. J.* **448**, L65-L68 (1995).
82. W. L. Freedman, B. F. Madore, B. K. Gibson, L. Ferrarese, D. D. Kelson, S. Sakai, J. R. Mould, R. C. Kennicutt, H. C. Ford, J. A. Graham, J. P. Huchra, S. M. G. Hughes, G. D. Illingworth, L. M. Macri, P. B. Stetson, Final results from the Hubble Space Telescope Key Project to measure the Hubble Constant. *Ap. J.* **553**, 47-72 (2001).
83. P. van Dokkum, R. Abraham, J. Brodie, C. Conroy, S. Danieli, A. Merritt, L. Mowla, A. Romanowsky, J. Zang, A high stellar velocity dispersion and ~100 globular clusters for the ultra-diffuse galaxy Dragonfly 44. *Ap. J. Lett.* **828**, L6 (2016).
84. P. McDonald, U. Seljak, S. Burles, D. J. Schlegel, D, H, Weinberg, D. Shih, J. Schaye, D. P. Schneider, J. Brinkmann, R. J. Brunner, M. Fukugita, The Lyman-alpha forest power spectrum from the Sloan Digital Sky Survey. *Ap. J.* **163**, 80-109 (2006).